Chinese Journal of Aeronautics, 2013,26(4): 967–975

Chinese Society of Aeronautics and Astronautics
& Beihang University

Chinese Journal of Aeronautics

cja@buaa.edu.cn
www.sciencedirect.com

Sliding mode control of reaction flywheel-based brushless DC motor with buck converter

Liu Gang *, Zhang Cong

School of Instrumentation Science and Opto-electronics Engineering, Beihang University, Beijing 100191, China

Received 21 March 2012; revised 29 May 2012; accepted 18 July 2012
Available online 30 April 2013

KEYWORDS

DC–DC converter;
Flywheels;
State averaging model;
Sliding mode control;
Sliding surface;
Topology

Abstract Reaction flywheel is a significant actuator for satellites' attitude control. To improve output torque and rotational speed accuracy for reaction flywheel, this paper reviews the modeling and control approaches of DC–DC converters and presents an application of the variable structure system theory with associated sliding regimes. Firstly, the topology of reaction flywheel is constructed. The small signal linearization process for a buck converter is illustrated. Then, based on the state averaging models and reaching qualification expressed by the Lee derivative, the general results of the sliding mode control (SMC) are analyzed. The analytical equivalent control laws for reaction flywheel are deduced detailedly by selecting various sliding surfaces at electromotion, energy consumption braking, reverse connection braking stages. Finally, numerical and experimental examples are presented for illustrative purposes. The results demonstrate that favorable agreement is established between the simulations and experiments. The proposed control strategy achieves preferable rotational speed regulation, strong rejection of modest disturbances, and high-precision output torque and rotational speed tracking abilities.

1. Introduction

With increasing complications and varieties of satellites, the requirement for attitude control becomes higher. As a significant actuator, a reaction flywheel has high output precision of angular momentum, strong anti-interference ability, and fast response, whose output torque accuracy directly affects attitude control precision. Thus, how to improve the stabilization and control precision for angular momentum is a key issue and urgent to be solved. The reaction flywheel can be regarded as a motor with a biggish moment of inertia. For the drive motor of reaction flywheel domestic and overseas, the brushless DC motor (BLDCM) is utilized widely with a relatively wide range of rotational speed, and the rotational speed regulation requires that the motor's line voltage changes with the rotational speed. Therefore, a voltage-mode controlled buck converter is mainly applied as a typical DC–DC converter. As is known, the DC–DC converter is a highly nonlinear plant with abundant dynamical behaviors, such as the Hopf bifurcation,[1] period doubling bifurcation,[2] border collision bifurcation,[3] tangent bifurcation,[4] coexisting attractors,[5] etc. The major difficulty in controlling the DC–DC converter is the exact modeling.

* Corresponding author. Tel.: +86 10 82317396.
E-mail addresses: liugang@buaa.edu.cn (G. Liu), haibou571@163.com (C. Zhang).

Peer review under responsibility of Editorial Committee of CJA.

ELSEVIER Production and hosting by Elsevier

1000-9361 © 2013 Production and hosting by Elsevier Ltd. on behalf of CSAA & BUAA. Open access under CC BY-NC-ND license.
http://dx.doi.org/10.1016/j.cja.2013.04.038

At present, the modeling approaches for DC–DC converters are generally divided into two types: one based on small signal analysis and the other using large signal analysis. The small signal analysis consists of the state-space averaging approach[6] and the averaged equivalent circuit approach.[7] However, the large signal analysis is complicated and also classified into two categories: one is based on the state-space averaging or circuit-average method, such as the phase plane method,[8] the switching signal flow graph approach,[9] etc.; the other uses state variables ripple determination, like the extended ripple analysis,[10] the *n*th harmonic three terminal model,[11] the Krylov Bogoliubov Mitropolskii (KBM) method,[12] the Volterra series determination,[13] the describing function method,[14] etc. Anyway, most control strategies are still based on the state-space averaging model or the linearization small signal model.

The DC–DC converter constitutes a closed-loop system with power stage and control circuit, whose topology determines the performance together with control strategy. Based on the average model, various control strategies have been investigated using feedback linearization, quasi-linear approach,[15] optimal control,[16] passivity techniques,[17] flatness methods,[18] H_∞ control,[19,20] linear multiloop control,[21] linear quadratic regulator (LQR) based control,[22] adaptive pole-zero position technique,[23] fuzzy control,[24,25] backstepping control,[26] etc. From the viewpoint of automatic control, the switching converter represents an interesting case study as a typical variable structure system (VSS). Especially, Sira-Ramirez[27]established an ideal equivalence among the pulse width modulation (PWM) and variable structure feedback options for nonlinear systems. Moreover, various sliding mode strategies have been developed extensively.[28–32] The sliding surface is made ideally invariant with respect to high-frequency switch controlled state trajectories. In order to improve the output torque accuracy and rotational speed tracking precision, the sliding mode control (SMC) technique of VSSs is applied to the reaction flywheel.

This paper is organized as follows: based on the state-space averaging approach, Section 2 analyzes the equivalent topologies of reaction flywheel and obtains its state averaging models at electromotion, energy consumption braking, and reverse connection braking stages, respectively; Section 3 briefly presents the general results of SMC for a typical variable structure system like the adopted buck converter; Section 4 is devoted to apply the results of Sections 2 and 3 to deduce detailedly the analytical equivalent control laws at different operation stages by selecting various sliding surfaces; Sections 5 and 6 describe simulations and experiments performed to verify the proposed strategy; Section 7 summarizes the conclusions.

2. Topology of reaction flywheel

The reaction flywheel is used to adjust the satellite attitude or counteract the disturbance torque to maintain the attitude stabilization with a reaction torque, which is produced by the motor's acceleration or deceleration. Fig. 1 shows the equivalent topology of reaction flywheel based on the BLDCM with a buck converter:

In Fig. 1, U_{DC} is power supply; VTp (p = 1 – 6) are commutation switching transistors, VT7 is a buck converter and VT8 an energy consumption braking transistor; VDq (q = 1 – 8) are anti-paralleled diodes; VD is a freewheeling diode, L a filter inductor, C a filter capacitor, i the input current of the inductor, i_m the line current of the motor, v capacitor voltage, R_p a power resistor, and R_s an accurate sampling resistor; R_m and L_m are equivalent resistor and inductor of windings, respectively; e_a, e_b, and e_c are the back electromotive force (EMF) of a, b, and c phase windings, respectively. With 3-phase 6-states wye-connected, each switching transistor of the upper and lower bridge is turned on simultaneously. Neglect the effect of commutation and assume that the 3-phase windings are symmetric with the same electric parameters.

Taking VT7-ON and VT8-OFF for example, the small signal linearization process for the adopted buck converter is illustrated as follows. Considering the buck converter only, using the continuous characteristic of inductor current and capacitor voltage yields

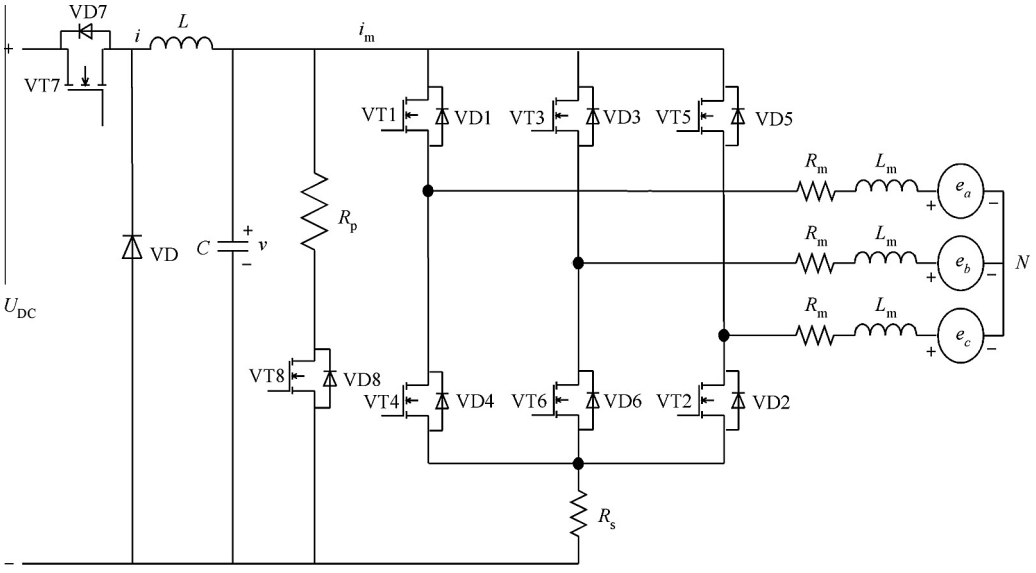

Fig. 1 Equivalent topology of reaction flywheel.

$$\begin{cases} i = C\frac{\mathrm{d}v}{\mathrm{d}t} = i_{T_s} - (i_m)_{T_s} \\ u = L\frac{\mathrm{d}i}{\mathrm{d}t} = (u_1)_{T_s}(U_{DC})_{T_s} - \Delta V_T - v_{T_s} \end{cases} \tag{1}$$

where i_{T_s}, $(i_m)_{T_s}$, $(u_1)_{T_s}$, $(U_{DC})_{T_s}$, and v_{T_s} are the average value of respective small signal i, i_m, u_1, U_{DC}, and v in a period T_s. Assuming that i_{T_s}, $(i_m)_{T_s}$, $(u_1)_{T_s}$, $(U_{DC})_{T_s}$, the forward voltage drop ΔV_T, and v_{T_s} are the sum of respective direct current signal and small signal, applying the small signal approximation yields

$$\begin{cases} (U_{DC})_{T_s} = \widehat{U}_{DC} + U_{DC}, (u_1)_{T_s} = u_1 + \hat{u}_1 \\ v_{T_s} = v + \hat{v}, i_{T_s} = i + \hat{i}, (i_m)_{T_s} = i_m + \hat{i}_m \end{cases} \tag{2}$$

where $\widehat{U}_{DC}$, $\hat{u}_1$, $\hat{v}$, $\hat{i}$, and $\hat{i}_m$ denote the respective direct current signal. Neglecting the high-order amount and utilizing the averaging approximation, the small signal model for the buck converter can be represented as

$$\begin{cases} C\frac{\mathrm{d}v}{\mathrm{d}t} = i - i_m \\ L\frac{\mathrm{d}i}{\mathrm{d}t} = u_1 U_{DC} - \Delta V_T - v \end{cases} \tag{3}$$

The reaction flywheel adopts electromotion at acceleration and energy consumption braking at deceleration, and switches to reverse connection braking at low speed. The technical measure saves the control energy and makes the drive circuit simple and reliable. However, this also means that three different topologies exist in the drive circuit: electromotion, energy consumption braking, and reverse connection braking. At present, the proportion-integral-derivative (PID) algorithm is mainly adopted at different operation states. In order to obtain fine accuracy, it takes engineers much time to choose appropriate control parameters at different operation states by experiments and experience. Nevertheless, it brings large disturbance in the states switching, inevitably. Moreover, SMC is a favorable switching feedback approach and a natural choice for switching converters, which is very suitable for buck converters.

Therefore, this paper adopts the SMC in the reaction flywheel. According to the characteristics of the specific plant, the analytical equivalent control laws are deduced detailedly at different operation states by selecting various sliding surfaces. In Sections 2.1–2.3, resorting to the averaging techniques, we describe the topologies of reaction flywheel at electromotion, energy consumption braking, and reverse connection braking stages, respectively, by taking a and b phase winding conducting as an example.

2.1. Topology at electromotion stage

Assuming the reaction flywheel operates in a continuous conduction mode, Fig. 2 displays the topology at the electromotion stage and its instantaneous model can be modeled as:

$$\begin{cases} C\frac{\mathrm{d}v}{\mathrm{d}t} = i - i_m \\ L\frac{\mathrm{d}i}{\mathrm{d}t} = u_1 U_{DC} - \Delta V_T - v \\ 2L_m\frac{\mathrm{d}i_m}{\mathrm{d}t} = v - 2\Delta V_T - (2R_m + R_s)i_m - K_e\omega \\ J\frac{\mathrm{d}\omega}{\mathrm{d}t} = K_t i_m - B_v\omega - T_d \end{cases} \tag{4}$$

where u_1 is the control input, J the moment of inertia, ω the rotational speed; K_t the torque coefficient, B_v the viscous friction coefficient; T_d the disturbance torque, and K_e the back EMF coefficient. As averaging is performed over cutting periods, the state variables x_1, x_2, x_3, and x_4 denote the average

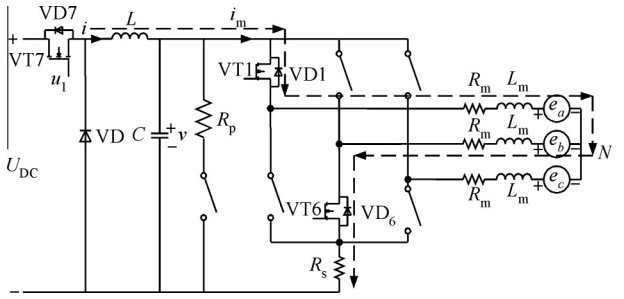

Fig. 2 Topology at eletromotion stage.

capacitor voltage, the average inductor current, the average line current, and the average rotational speed, respectively, i.e., $x_1 = v$, $x_2 = i$, $x_3 = i_m$, and $x_4 = \omega$. The control input u_1 (called duty ratio) is in turn the average value of the actual binary-type control signals. Its state averaging model can be expressed as

$$\dot{\boldsymbol{x}} = \begin{bmatrix} \dot{x}_1 \\ \dot{x}_2 \\ \dot{x}_3 \\ \dot{x}_4 \end{bmatrix} = \begin{bmatrix} 0 & \frac{1}{C} & -\frac{1}{C} & 0 \\ -\frac{1}{L} & 0 & 0 & 0 \\ \frac{1}{2L_m} & 0 & -\frac{2R_m+R_s}{2L_m} & -\frac{K_e}{2L_m} \\ 0 & 0 & \frac{K_t}{J} & -\frac{B_v}{J} \end{bmatrix} \boldsymbol{x} + \begin{bmatrix} 0 \\ \frac{U_{DC}}{L} \\ 0 \\ 0 \end{bmatrix} u_1 + \begin{bmatrix} 0 \\ \frac{-\Delta V_T}{L} \\ \frac{-\Delta V_T}{L_m} \\ -\frac{T_d}{J} \end{bmatrix} \tag{5}$$

2.2. Topology at energy consumption braking stage

Turning off the power supply, the back EMF makes the current loop form controlled reverse braking current by the energy consumption resistor R_p, the switching transistor VT8, and the anti-paralleled diodes VD1 and VD6, while the motor runs in the power generation mode. Assuming it operates in the continuous conduction mode, Fig. 3 reveals the topology at the energy consumption braking stage and its instantaneous model can be denoted as:

$$\begin{cases} 2L_m\frac{\mathrm{d}i_m}{\mathrm{d}t} = u_2 K_e\omega - \Delta V_T - 2\Delta V_D - (2R_m + R_p + R_s)i_m \\ J\frac{\mathrm{d}\omega}{\mathrm{d}t} = -K_t i_m - B_v\omega - T_d \end{cases} \tag{6}$$

where u_2 is the control input and ΔV_D is the forward voltage drop of the anti-paralleled diode VD. As averaging is performed over cutting periods, let state variables $x_1 = i_m$ and $x_2 = \omega$. Its state averaging model is derived as follows:

$$\dot{\boldsymbol{x}} = \begin{bmatrix} \dot{x}_1 \\ \dot{x}_2 \end{bmatrix} = \begin{bmatrix} -\frac{2R_m+R_p+R_s}{L_m} & 0 \\ -\frac{K_t}{J} & -\frac{B_v}{J} \end{bmatrix} \boldsymbol{x} + \begin{bmatrix} \frac{K_e x_2}{2L_m} \\ 0 \end{bmatrix} u_2 + \begin{bmatrix} -\frac{\Delta V_T + 2\Delta V_D}{2L_m} \\ -\frac{T_d}{J} \end{bmatrix} \tag{7}$$

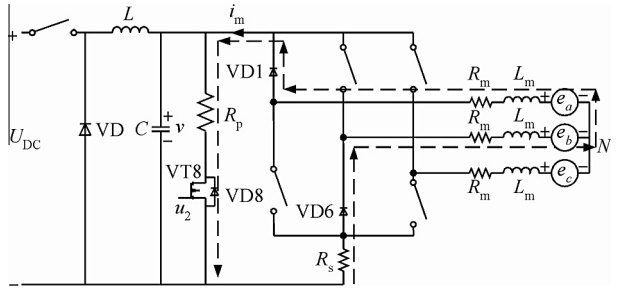

Fig. 3 Topology at energy consumption braking stage.

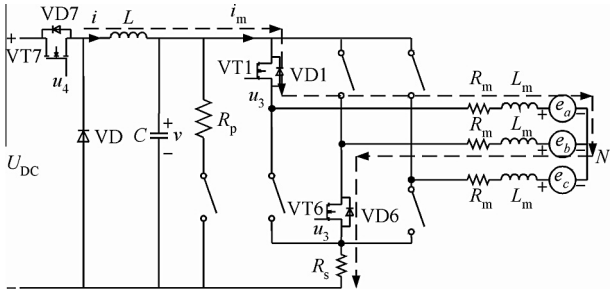

Fig. 4 Topology at reverse connection braking stage.

2.3. Topology at reverse connection braking stage

The braking power is provided with power supply and the buck converter outputs constant capacitor voltage v at the reverse connection braking stage, which must satisfy $v > K_e\omega + \Delta V_T$ to eliminate the interphase internal circulation of windings. Besides, the commutation switching transistors VT1 and VT6 execute pulse width modulation in respective conduction region to regulate the braking torque as in Fig. 4 and its instantaneous model can be derived as

$$\begin{cases} C\frac{dv}{dt} = i - i_m \\ L\frac{di}{dt} = u_4 U_{DC} - \Delta V_T - v \\ 2L_m\frac{di_m}{dt} = u_3(v + K_e\omega) - 2\Delta V_T - (2R_m + R_s)i_m \\ J\frac{d\omega}{dt} = -K_t i_m - B_v\omega - T_d \end{cases} \tag{8}$$

As averaging is performed over cutting periods, let state variables $x_1 = v$, $x_2 = i$, $x_3 = i_m$, and $x_4 = \omega$. Its state averaging model is described as

$$\dot{\boldsymbol{x}} = \begin{bmatrix} \dot{x}_1 \\ \dot{x}_2 \\ \dot{x}_3 \\ \dot{x}_4 \end{bmatrix} = \begin{bmatrix} 0 & \frac{1}{C} & -\frac{1}{C} & 0 \\ -\frac{1}{L} & 0 & 0 & 0 \\ 0 & 0 & -\frac{2R_m+R_s}{2L_m} & 0 \\ 0 & 0 & -\frac{K_t}{J} & -\frac{B_v}{J} \end{bmatrix} \boldsymbol{x} + \begin{bmatrix} 0 \\ \frac{U_{DC}}{L} \\ 0 \\ 0 \end{bmatrix} u_4 + \begin{bmatrix} 0 \\ 0 \\ \frac{x_1+K_e x_4}{2L_m} \\ 0 \end{bmatrix} u_3 + \begin{bmatrix} 0 \\ \frac{-\Delta V_T}{L} \\ \frac{-\Delta V_T}{L_m} \\ -\frac{T_d}{J} \end{bmatrix} \tag{9}$$

where u_3 and u_4 are the control inputs.

The output torque T_o of the reaction flywheel is proportional to the derivative of rotational speed ω, i.e., $T_o = J\dot{\omega}$. According to the action and reaction law, the reaction torque on the satellite is equal to T_o, but with an opposite sign.

3. General results of SMC

Sira-Ramirez[27] presented a differential geometric approach for design of sliding modes in nonlinear VSSs, coordinate-free characterizations of local existence conditions for sliding regimes, and a geometric reformulation of some of its most salient features. Moreover, he also demonstrated the existence of an ideal equivalence among SMC and PWM control response in nonlinear dynamical systems.[33] Similarly, consider the following smooth nonlinear system:

$$\dot{\boldsymbol{x}} = \boldsymbol{f}(\boldsymbol{x}) + \boldsymbol{g}(\boldsymbol{x})u \tag{10}$$

where $\boldsymbol{x} \in \boldsymbol{X}$, an open set of $\mathbf{R}^n$, the scalar control input u: $\mathbf{R}^n \to \mathbf{R}$ is a feedback control function, while $\boldsymbol{f}$ and $\boldsymbol{g}$ are smooth local vector fields defined on $\boldsymbol{X}$ with $\boldsymbol{g}(\boldsymbol{x}) \neq \boldsymbol{0}$ and $\forall \boldsymbol{x} \in \boldsymbol{X}$. Let s denote a smooth real value of $\boldsymbol{x}$ defined by s:$\boldsymbol{X} \to \mathbf{R}$. The level set $\boldsymbol{S} = \{\boldsymbol{x} \in \mathbf{R}^n: s(\boldsymbol{x}) = 0\}$, defines a locally regular $n-1$ dimensional sub-manifold, addressed as the sliding surface.

Without loss of generality, a SMC control law that accomplishes the surface reachability is obtained by letting u take one of two possible values, namely 0 or 1. According to Ref. [34], u can be selected as:

$$u = \begin{cases} 0.5(1 + \mathrm{sgn}(s)) & L_g s = \langle \mathrm{d}s, \boldsymbol{g} \rangle < 0 \\ 0.5(1 - \mathrm{sgn}(s)) & L_g s = \langle \mathrm{d}s, \boldsymbol{g} \rangle > 0 \end{cases} \tag{11}$$

where ds denotes the one-form corresponding to the gradient of $s(\boldsymbol{x})$, that is assumed to be nonzero in $\boldsymbol{X}$ except $<,>$ is the standard scalar product. In the method of equivalent control, ideal sliding motions are described by using the manifold invariance conditions $s = 0$ and $L_{f+u_{eq}g}s = 0$, where u_{eq} is a smooth equivalent control law, explicitly given by:[27]

$$u_{eq} = -\frac{L_f s}{L_g s} = -\frac{\langle \mathrm{d}s, \boldsymbol{f} \rangle}{\langle \mathrm{d}s, \boldsymbol{g} \rangle} = -\left(\frac{\mathrm{d}s}{\mathrm{d}\boldsymbol{x}}\boldsymbol{f}\right)\left(\frac{\mathrm{d}s}{\mathrm{d}\boldsymbol{x}}\boldsymbol{g}\right)^{-1} \tag{12}$$

A necessary and sufficient condition for the equivalent control to be well defined is represented by the transversality condition $L_g s \neq 0$.[33] Meanwhile, a sliding regime exists on $\boldsymbol{S}$ if and only if for all $\boldsymbol{x} \in \boldsymbol{S}$ the equivalent control satisfies $0 < u_{eq} < 1$.[34]

4. Equivalent control law design

In this paper, the output torque of reaction flywheel is implemented by controlling the rotational speed of the BLDCM. The BLDCM adopts 3-phase full bridge topology with a buck converter. In order to achieve 4-quadrant operation for the BLDCM, the rotational speed is changed by regulating the duty ratio for the buck converter's switching diodes VT7 and VT8. In the buck converter, the duty ratio belongs to control limited situation. Therefore, the design of the buck converter controller focuses on selection of the sliding surface and derivation of the sliding mode control law for u_1, u_2, u_3, and u_4 at different quadrants. The sliding surface is important to the control precision of the reaction flywheel. The sliding surface must make sure that all the measurable states are included in the sliding surface, and the actual rotational speed can track the rotational speed command with first-order transition dynamic.

By searching a dominating set, the SMC of reaction flywheel utilizes the states discrepancy of the buck converter to reach the sliding surface as quickly as possible during the continuous conduction mode, which satisfies the asymptotic stability criteria with preferable dynamics performance. However, the control input is 0 or 1, which is confined strictly. Therefore, most SMC designs concentrate on the selection of sliding surfaces. In this section, we deduce detailedly the analytical equivalent control laws at electromotion, energy consumption braking, and reverse connection braking stages by selecting different sliding surfaces, respectively.

In general, we should choose sliding surfaces and appropriate coefficients to guarantee the sliding mode stability and favorable dynamic performance based on the anticipant control object. According to the state averaging models, the

sliding surfaces are selected as $s_1(\boldsymbol{x})$, $s_2(\boldsymbol{x})$, and $s_3(\boldsymbol{x})$ at electromotion, energy consumption braking, and reverse connection braking stages, respectively.

4.1. Equivalent control law at electromotion stage

According to Eq. (5), we have

$$\boldsymbol{f}_1(\boldsymbol{x})=\begin{bmatrix}0 & \frac{1}{C} & -\frac{1}{C} & 0\\ -\frac{1}{L} & 0 & 0 & 0\\ \frac{1}{2L_\mathrm{m}} & 0 & -\frac{2R_\mathrm{m}+R_\mathrm{s}}{2L_\mathrm{m}} & -\frac{K_\mathrm{e}}{2L_\mathrm{m}}\\ 0 & 0 & \frac{K_\mathrm{t}}{J} & -\frac{B_\mathrm{v}}{J}\end{bmatrix}\boldsymbol{x},\quad \boldsymbol{g}_1(\boldsymbol{x})=\begin{bmatrix}0\\ \frac{U_\mathrm{DC}}{L}\\ 0\\ 0\end{bmatrix} \tag{13}$$

Here, the sliding surface is selected as:

$$\begin{aligned}s_1(\boldsymbol{x})=&[c_1(v_\mathrm{r}-x_1)+(\dot{v}_\mathrm{r}-\dot{x}_1)]+[c_2(i_\mathrm{mr}-x_3)+(\dot{i}_\mathrm{mr}-\dot{x}_3)]\\&+[c_3(\omega_\mathrm{r}-x_4)+(\dot{\omega}_\mathrm{r}-\dot{x}_4)]\end{aligned} \tag{14}$$

where c_1, c_2, and c_3 are control parameters, v_r is the referenced capacitor voltage, i_mr the referenced line current, and ω_r the referenced rotational speed. Assuming v_r, i_mr, and ω_r are constants in the continuous conduction mode, then

$$\begin{aligned}s_1(\boldsymbol{x})=&-\left(c_1+\frac{1}{2L_\mathrm{m}}\right)x_1-\frac{1}{C}x_2-\left(c_2-\frac{1}{C}-\frac{2R_\mathrm{m}+R_\mathrm{s}}{2L_\mathrm{m}}+\frac{K_\mathrm{t}}{J}\right)x_3\\&-\left(c_3-\frac{K_\mathrm{e}}{2L_\mathrm{m}}-\frac{B_\mathrm{v}}{J}\right)x_4\\&+\left(c_1v_\mathrm{r}+c_2i_\mathrm{mr}+c_3\omega_\mathrm{r}+\frac{\Delta V_\mathrm{T}}{L_\mathrm{m}}+\frac{T_\mathrm{d}}{J}\right)\end{aligned} \tag{15}$$

Let $A_1=c_1+\frac{1}{2L_\mathrm{m}}$, $A_2=\frac{1}{C}$, $A_3=c_2-\frac{1}{C}-\frac{2R_\mathrm{m}+R_\mathrm{s}}{2L_\mathrm{m}}+\frac{K_\mathrm{t}}{J}$, $A_4=c_3-\frac{K_\mathrm{e}}{2L_\mathrm{m}}-\frac{B_\mathrm{v}}{J}$, and $D=c_1v_\mathrm{r}+c_2i_{mr}+c_3\omega_\mathrm{r}+\frac{\Delta V_\mathrm{T}}{L_\mathrm{m}}+\frac{T_\mathrm{d}}{J}$. Eq. (15) can be simplified as $s_1(\boldsymbol{x})=-A_1x_1-A_2x_2-A_3x_3-A_4x_4+D$.

With Eqs. (11) and (13), then

$$L_{\boldsymbol{g}_1}s=\langle \mathrm{d}s,\boldsymbol{g}_1\rangle=\begin{bmatrix}\frac{\partial s_1}{\partial x_1} & \frac{\partial s_1}{\partial x_2} & \frac{\partial s_1}{\partial x_3} & \frac{\partial s_1}{\partial x_4}\end{bmatrix}\boldsymbol{g}_1(\boldsymbol{x})=-\frac{U_\mathrm{DC}}{CL}<0 \tag{16}$$

The control input u_1 can be specified as $u_1=0.5(1+\mathrm{sgn}(s))$. By exploiting Eqs. (12) and (13), we have

$$\begin{aligned}u_{1\mathrm{eq}}=&-\frac{L_{f_1}s}{L_{\boldsymbol{g}_1}s}=\left(-\frac{CL}{U_\mathrm{DC}}\right)\left\{\left(\frac{A_3}{2L_\mathrm{m}}-\frac{A_2}{L}\right)x_1+\frac{A_1}{C}x_2\right.\\&\left.+\left[\frac{K_\mathrm{t}A_4}{J}-\frac{A_1}{C}-\frac{(2R_\mathrm{m}+R_\mathrm{s})A_3}{2L_\mathrm{m}}\right]x_3-\left(\frac{K_\mathrm{e}A_3}{2L_\mathrm{m}}+\frac{B_\mathrm{v}A_4}{J}\right)x_4\right\}\end{aligned} \tag{17}$$

Let $s_1(\boldsymbol{x})=0$, then $x_2=-\frac{A_1}{A_2}x_1-\frac{A_3}{A_2}x_3-\frac{A_4}{A_2}x_4+\frac{D}{A_2}$. Substituting this x_2 expression into Eq. (17) yields

$$\begin{aligned}u_{1\mathrm{eq}}=&-\frac{CL}{U_\mathrm{DC}}\left\{\left(\frac{A_3}{2L_\mathrm{m}}-\frac{A_2}{L}-\frac{A_1^2}{CA_2}\right)x_1\right.\\&+\left[\frac{K_\mathrm{t}A_4}{J}-\frac{A_1}{C}-\frac{A_1A_3}{CA_2}-\frac{(2R_\mathrm{m}+R_\mathrm{s})A_3}{2L_\mathrm{m}}\right]x_3\\&\left.-\left(\frac{K_\mathrm{e}A_3}{2L_\mathrm{m}}+\frac{B_\mathrm{v}A_4}{J}+\frac{A_1A_4}{CA_2}\right)x_4+\frac{DA_1}{CA_2}\right\}\end{aligned} \tag{18}$$

4.2. Equivalent control law at energy consumption braking stage

According to Eq. (7), we have

$$\boldsymbol{f}_2(\boldsymbol{x})=\begin{bmatrix}-\frac{2R_\mathrm{m}+R_\mathrm{p}+R_\mathrm{s}}{L_\mathrm{m}} & 0\\ -\frac{K_\mathrm{t}}{J} & -\frac{B_\mathrm{v}}{J}\end{bmatrix}\boldsymbol{x},\quad \boldsymbol{g}_2(\boldsymbol{x})=\begin{bmatrix}\frac{K_\mathrm{e}x_2}{2L_\mathrm{m}}\\ 0\end{bmatrix} \tag{19}$$

Here, the sliding surface is selected as:

$$s_2(\boldsymbol{x})=c_1(\omega_\mathrm{r}-x_2)+(\dot{\omega}_\mathrm{r}-\dot{x}_2) \tag{20}$$

Assuming ω_r is a constant, then

$$s_2(\boldsymbol{x})=\frac{K_\mathrm{t}}{J}x_1+\left(-c_1+\frac{B_\mathrm{v}}{J}\right)x_2+\frac{T_\mathrm{d}}{J} \tag{21}$$

With Eqs. (19) and (21), then

$$L_{\boldsymbol{g}_2}s=\langle \mathrm{d}s,\boldsymbol{g}_2\rangle=\frac{K_\mathrm{t}K_\mathrm{e}x_2}{2JL_\mathrm{m}}>0 \tag{22}$$

The control input u_2 can be described as $u_2=0.5(1-\mathrm{sgn}(s))$. By exploiting Eqs. (19) and (22), the following equation holds:

$$\begin{aligned}u_{2\mathrm{eq}}=&-\frac{L_{f_2}s}{L_{\boldsymbol{g}_2}s}=\frac{2L_\mathrm{m}}{K_\mathrm{t}K_\mathrm{e}x_2}\\&\times\left[\frac{JK_\mathrm{t}(2R_\mathrm{m}+R_\mathrm{p}+R_\mathrm{s})-c_1K_\mathrm{t}JL_\mathrm{m}+K_\mathrm{t}B_\mathrm{v}L_\mathrm{m}}{JL_\mathrm{m}}x_1\right.\\&\left.+\frac{B_\mathrm{v}(B_\mathrm{v}-c_1J)}{J}x_2\right]\end{aligned} \tag{23}$$

Let $s_2(\boldsymbol{x})=0$, then $x_1=-\frac{J}{K_\mathrm{t}}\left[\left(-c_1+\frac{B_\mathrm{v}}{J}\right)x_2+\frac{T_\mathrm{d}}{J}\right]$. Substituting this x_1 expression into Eq. (23) yields

$$\begin{aligned}u_{2\mathrm{eq}}=&\frac{2[JK_\mathrm{t}(2R_\mathrm{m}+R_\mathrm{p}+R_\mathrm{s})-c_1K_\mathrm{t}JL_\mathrm{m}+K_\mathrm{t}B_\mathrm{v}L_\mathrm{m}]x_1}{JK_\mathrm{t}K_\mathrm{e}x_2}\\&+\frac{2L_\mathrm{m}B_\mathrm{v}(B_\mathrm{v}-c_1J)}{JK_\mathrm{t}K_\mathrm{e}}\end{aligned} \tag{24}$$

4.3. Equivalent control law at reverse connection braking stage

According to Eq. (9), we have

$$\begin{cases}\boldsymbol{f}_3(\boldsymbol{x})=\begin{bmatrix}0 & \frac{1}{C} & -\frac{1}{C} & 0\\ -\frac{1}{L} & 0 & 0 & 0\\ 0 & 0 & -\frac{2R_\mathrm{m}+R_\mathrm{s}}{2L_\mathrm{m}} & 0\\ 0 & 0 & -\frac{K_\mathrm{t}}{J} & -\frac{B_\mathrm{v}}{J}\end{bmatrix}\boldsymbol{x}\\ \boldsymbol{g}(\boldsymbol{x})=\boldsymbol{g}_4(\boldsymbol{x})+\boldsymbol{g}_3(\boldsymbol{x})=\begin{bmatrix}0\\ \frac{U_\mathrm{DC}}{L}\\ 0\\ 0\end{bmatrix}+\begin{bmatrix}0\\ 0\\ \frac{x_1+K_\mathrm{e}x_4}{2L_\mathrm{m}}\\ 0\end{bmatrix}\end{cases} \tag{25}$$

Here, the sliding surface is selected as:

$$s_3(\boldsymbol{x})=[c_1(v_\mathrm{r}-x_1)+(\dot{v}_\mathrm{r}-\dot{x}_1)]+[c_2(\omega_\mathrm{r}-x_4)+(\dot{\omega}_\mathrm{r}-\dot{x}_4)] \tag{26}$$

Assuming that v_r and ω_r are constants, then

$$\begin{aligned}s_3(\boldsymbol{x})=&-c_1x_1-\frac{1}{C}x_2+\left(\frac{1}{C}+\frac{K_\mathrm{t}}{J}\right)x_3-\left(c_2-\frac{B_\mathrm{v}}{J}\right)x_4\\&+\left(c_1v_\mathrm{r}+c_2\omega_\mathrm{r}+\frac{T_\mathrm{d}}{J}\right)\end{aligned} \tag{27}$$

With Eqs. (11) and (27), then

$$L_{\boldsymbol{g}_4}s=\langle \mathrm{d}s,\boldsymbol{g}_4\rangle=-\frac{U_\mathrm{DC}}{CL}<0 \tag{28}$$

The control input u_4 can be described as $u_4=0.5(1+\mathrm{sgn}(s))$. By exploiting Eqs. (12) and (25), we have

$$u_{4\mathrm{eq}} = -\frac{L_{f_3}s}{L_{g_4}s} = \frac{U_{\mathrm{DC}}}{CL}\left[\frac{1}{CL}x_1 - \frac{c_1}{C}x_2 + \frac{B_{\mathrm{v}}(c_2J - B_{\mathrm{v}})}{J^2}x_4 - \frac{-2c_1J^2L_{\mathrm{m}} + J(2R_{\mathrm{m}} + R_{\mathrm{s}})(J + K_{\mathrm{t}}C) - 2K_{\mathrm{t}}CL_{\mathrm{m}}(c_2J - B_{\mathrm{v}})}{2CJ^2L_{\mathrm{m}}}x_3\right] \tag{29}$$

Let $s_3(\boldsymbol{x}) = 0$, then $x_2 = -c_1Cx_1 + (1 + \frac{K_{\mathrm{t}}C}{J})x_3 - C(c_2 - \frac{B_{\mathrm{v}}}{J})x_4 + C(c_1v_{\mathrm{r}} + c_2\omega_{\mathrm{r}} + \frac{T_{\mathrm{d}}}{J})$. Substituting the x_2 expression into Eq. (29) yields

$$u_{4\mathrm{eq}} = \frac{CL}{U_{\mathrm{DC}}}\left[\left(\frac{1}{CL} + c_1^2\right)x_1 - \frac{J(2R_{\mathrm{m}} + R_{\mathrm{s}})(J + K_{\mathrm{t}}C) - 2K_{\mathrm{t}}CL_{\mathrm{m}}(c_2J - B_{\mathrm{v}}) + 2c_1K_{\mathrm{t}}CJL_{\mathrm{m}}}{2CJ^2L_{\mathrm{m}}}x_3 + \frac{B_{\mathrm{v}}(c_2J - B_{\mathrm{v}}) + c_1J(c_2J - B_{\mathrm{v}})}{J^2}x_4 - c_1\left(c_1v_{\mathrm{r}} + c_2\omega_{\mathrm{r}} + \frac{T_{\mathrm{d}}}{J}\right)\right] \tag{30}$$

Using the same procedure, we have

$$L_{g_3}s = \langle \mathrm{d}s, \boldsymbol{g}_3\rangle = \left(\frac{1}{C} + \frac{K_{\mathrm{t}}}{J}\right)\left(\frac{x_1 + K_{\mathrm{e}}x_4}{2L_{\mathrm{m}}}\right) > 0 \tag{31}$$

The control input u_3 can be denoted as $u_3 = 0.5(1 - \mathrm{sgn}(s))$. By exploiting Eqs. (12) and (25), we have

$$u_{3\mathrm{eq}} = -\frac{L_{f_3}s}{L_{g_3}s} = \frac{2CJL_{\mathrm{m}}}{(J + K_{\mathrm{t}}C)(x_1 + K_{\mathrm{e}}x_4)} \times \left[-\frac{1}{CL}x_1 + \frac{c_1}{C}x_2 - \frac{B_{\mathrm{v}}(c_2J - B_{\mathrm{v}})}{J^2}x_4 + \frac{-2c_1J^2L_{\mathrm{m}} + J(2R_{\mathrm{m}} + R_{\mathrm{s}})(J + K_{\mathrm{t}}C) - 2K_{\mathrm{t}}CL_{\mathrm{m}}(c_2J - B_{\mathrm{v}})}{2CJ^2L_{\mathrm{m}}}x_3\right] \tag{32}$$

Substituting the x_2 expression into Eq. (32) yields

$$u_{3\mathrm{eq}} = \frac{2CJL_{\mathrm{m}}}{(J + K_{\mathrm{t}}C)(x_1 + K_{\mathrm{e}}x_4)}\left\{-\left(\frac{1}{CL} + c_1^2\right)x_1 + \left[\frac{J(2R_{\mathrm{m}} + R_{\mathrm{s}})(J + K_{\mathrm{t}}C) - 2K_{\mathrm{t}}CL_{\mathrm{m}}(c_2J - B_{\mathrm{v}})}{2CJ^2L_{\mathrm{m}}} + \frac{2c_1K_{\mathrm{t}}CJL_{\mathrm{m}}}{2CJ^2L_{\mathrm{m}}}\right]x_3 - \frac{B_{\mathrm{v}}(c_2J - B_{\mathrm{v}}) + c_1J(c_2J - B_{\mathrm{v}})}{J^2}x_4 + c_1\left(c_1v_{\mathrm{r}} + c_2\omega_{\mathrm{r}} + \frac{T_{\mathrm{d}}}{J}\right)\right\} \tag{33}$$

By selecting appropriate parameters c_1, c_2, and c_3, Eqs. (18), (24), (30), and (33) meet the transversal and sliding mode existence conditions. In this paper, the saturation function sat(·) is used to substitute the ideal switching function sgn(·) to weaken the chattering and low-pass filtering is carried out for the control input. Furthermore, the sliding mode motion is divided into the reaching and sliding stages. The frequent switching among the two stages produces high frequency chattering. Hence, as the rotational speed tracking error is large, the proposed sliding mode controller is adopted to improve the dynamic performance. However, when the sliding motion reaches the sliding surface, a conventional PID controller can be chosen to overcome the chattering.

5. Simulations

A scheme of the simulation setup of the reaction flywheel system for measuring and regulating is demonstrated with the PID and SMC algorithms respectively, shown in Fig. 5. According to the output torque equation, the referenced torque instructions T_{r} are transformed to the referenced rotational speed ω_{r}.

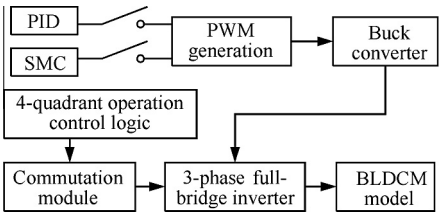

Fig. 5 Simulation model.

Moreover, the referenced capacitor voltage is set as $v_{\mathrm{r}} = 12$ V at the reverse connection braking stage. Meanwhile, the disturbance torque for the simulation model is considered as a Gaussian stochastic disturbance with maximum 0.004 N·m. The key electric parameters for the simulation model are based on the design values, calculated values, or experimental measurements, listed in Table 1.

To meet the transversal and sliding mode existence conditions, the control parameters are selected as follows: at the electromotion stage, $c_1 = 0.25$, $c_2 = 0.01$, and $c_3 = 0.0036$; at the energy consumption braking stage, $c_1 = 0.027$; at the reverse connection braking stage, $c_1 = 0.18$ and $c_2 = 0.037$. Table 2 illustrates the 4-quadrant operation control logic of the reaction flywheel BLDCM.

Supposing that the torque instructions T_{r} are 0.04 N·m and −0.04 N·m alternately, the reaction flywheel simulation model operates circularly under the 4-quadrant operation control logic of the BLDCM. Fig. 6 shows the rotational speed instructions ω_{r}, the actual rotational speed ω, and the rotational speed error $\omega - \omega_{\mathrm{r}}$ curves with the PID and

Table 1 Key electric parameters.

Parameter	Value	Parameter	Value
J (kg·m^2)	0.0135	$R_{\mathrm{p}}(\Omega)$	5.1
K_{t} (N·m/A)	0.021	$R_{\mathrm{s}}(\Omega)$	0.11
K_{e} (V·r/min)	0.00167	L(mH)	0.63
B_{v} (N·m/(rad/s))	0.00021	C(μF)	47
L_{m}(μH)	53	ΔV_{T}, ΔV_{D}(V)	0.7
$R_{\mathrm{m}}(\Omega)$	0.17	U_{DC}(V)	28

Table 2 Four-quadrant operation control logic of reaction flywheel BLDCM.

T_{r}	Rotational direction	Rotational speed(r/min)	Operation stage
+	Counterclockwise	0–5000	Electromotion stage
	Clockwise	−5000 to −3000	Energy consumption braking stage
		−3000–0	Reverse connection braking stage
−	Clockwise	0 to −5000	Electromotion stage
	Counterclockwise	5000–3000	Energy consumption braking stage
		3000–0	Reverse connection braking stage

the SMC, respectively. Fig. 7 presents the corresponding torque instructions T_r, the output torque T_o, and the torque error T_o-T_r curves with the PID and the SMC, respectively.

The simulation results indicate that, compared with the PID, the SMC algorithm is more robust to the Gaussian stochastic disturbance torque. Its rotational speed tracking error is less than 2 r/min and the output torque tracking error is less than 0.0015 N·m in the whole rotational speed range. In addition, due to the effect of the Gaussian stochastic disturbance torque, the output torque tracking error increases from less than 0.001 N·m to about 0.0015 N·m at zero-crossing rotational speed.

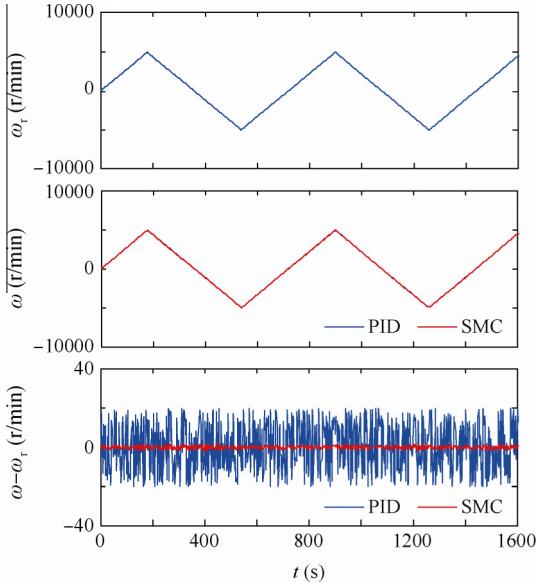

Fig. 6 Rotational speed response curves at simulation.

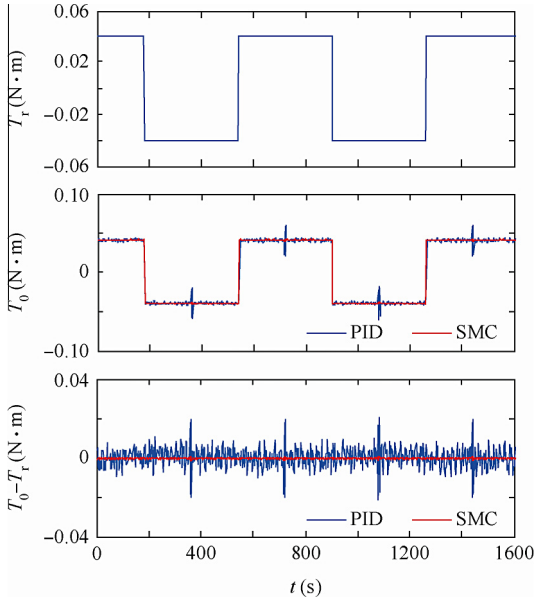

Fig. 7 Torque response curves at simulation.

6. Experiments

The motor structure and magnetic circuit design is taken into account to minimize the required winding current, while ensuring the maximum output torque. The heat dissipation in the motor is through conduction and radiation. Moreover, the reaction flywheel prototype is kept in a vacuum chamber (<10 Pa) for long-running with a full load. The experimental results show that the motor temperature stabilizes at about 56 °C and keeps balance, so the heat in the motor does not influence its normal operation.

To demonstrate the effectiveness of the SMC algorithm proposed in this paper, the corresponding control system is constructed. Fig. 8 represents the reaction flywheel prototype and the vacuum chamber. The major technical indices of the reaction flywheel prototype are listed in Table 3.

According to the numerical calculation and simulation validation, a set of control parameters are selected to satisfy the transversal and sliding mode existence conditions: at the electromotion stage, $c_1 = 0.22$, $c_2 = 0.008$, and $c_3 = 0.0033$; at the energy consumption braking stage, $c_1 = 0.025$; at the reverse connection braking stage, $c_1 = 0.16$ and $c_2 = 0.043$. The reaction flywheel prototype starts up with counterclockwise electromotion until a rated rotational speed of 5000 r/min as T_r is 0.04 N·m. Then, T_r changes from 0.04 N·m to −0.04 N·m and the reaction flywheel operates at the counterclockwise energy consumption braking stage. When ω reaches 3000 r/min, the reaction flywheel transforms to the reverse connection braking stage until it stops and commences with a clockwise movement. Fig. 9 displays ω_r, ω, and $\omega-\omega_r$ curves with the PID and the SMC, respectively. Fig. 10 shows the corresponding T_r, T_o, and T_o-T_r curves with the PID and the SMC, respectively.

The above experimental curves show that the SMC algorithm excels in the output torque tracking accuracy and rotational speed tracking precision with fast response and preferable dynamic performance. The rotational speed tracking error is less than 2 r/min and the output torque tracking error is less than 0.001 N·m. In addition, the disturbance

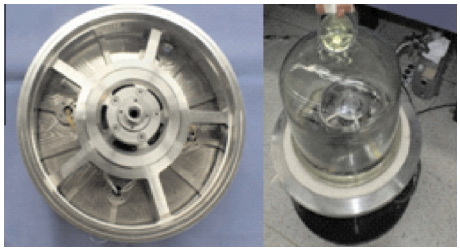

Fig. 8 Reaction flywheel prototype and vacuum chamber.

Table 3 Major technical indices.

Parameter	Value
Maximum power dissipation (W)	80
Angular momentum (N·m·s)	15
Maximum rotational speed (r/min)	6000
Rated rotational speed (r/min)	5000
Maximum output torque (N·m)	0.06

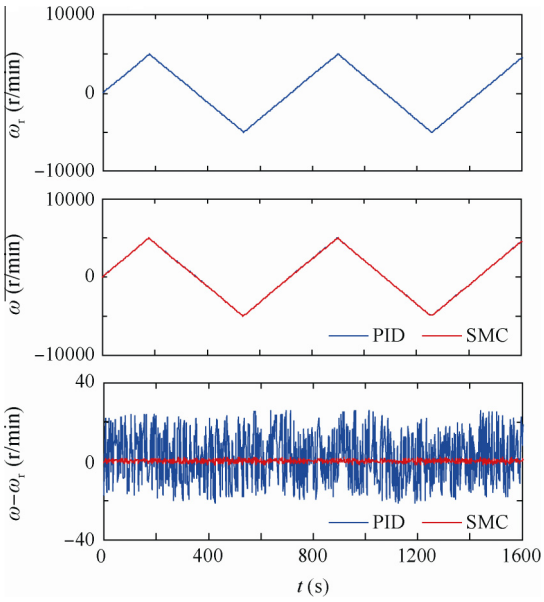

Fig. 9 Rotational speed response curves at experimentation.

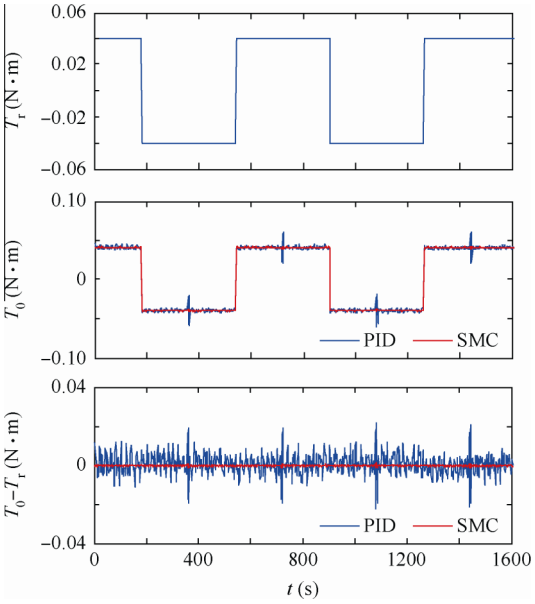

Fig. 10 Torque response curves at experimentation.

torque is restrained effectively. However, the output torque tracking error still increases at zero-crossing rotational speed, because the installed switching Hall sensors in the experiments are not good enough to measure the rotational speed accurately at low speed.

7. Conclusions

(1) The reaction flywheel simulation results are consistent with the prototype experimental results. Compared with the PID, the SMC algorithm is more robust to the Gaussian stochastic disturbance torque, which is restrained effectively.

(2) The SMC algorithm improves the output torque tracking accuracy and rotational speed tracking precision of reaction flywheel with fast response and preferable dynamic performance.

(3) When the referenced torque instructions T_r are $\pm$ 0.04 N·m, the rotational speed tracking error is less than 2 r/min and the output torque tracking error is less than 0.001 N·m with the proposed SMC algorithm.

Acknowledgement

This study was supported by the National Natural Science Foundation of China (No. 61121003).

References

1. Kavitha A, Uma G. Experimental verification of hopf bifurcation in DC–DC Luo converter. *IEEE Trans Power Electron* 2008;**23**(6):2878–83.
2. El-Aroudi A, Rodriquez E, Leyva R, Alarcon E. A design-oriented combined approach for bifurcation prediction in switched-mode power converters. *IEEE Trans Circuits Syst Express Briefs* 2010;**57**(3):218–22.
3. Maity S, Tripathy D, Bhattacharya TK, Banerjee S. Bifurcation analysis of PWM-1 voltage-mode controlled buck converter using the exact discrete model. *IEEE Trans Circuits Syst Regul Pap* 2007;**54**(5):1120–30.
4. Zhou YF, Chen JN. Tangent bifurcation and intermittent chaos in current-mode controlled boost converters. *Proc CSEE* 2005;**25**(1):23–6 [Chinese].
5. Zhou YF, Chen JN, Xu C. Simulation and experimental studies on coexisting attractors in DC–DC switching converter. *Proc CSEE* 2011;**25**(21):1–6 [Chinese].
6. Davoudi A, Jatskevich JJ. Parasitics realization in state-space average-value modeling of PWM DC–DC converters using an equal area method. *IEEE Trans Circuits Syst Regul Pap* 2007;**54**(9):1960–7.
7. Van-Dijk E, Spruijt HJN, O'Sullivan DM, Klaassens JB. PWM-switch modeling of DC–DC converters. *IEEE Trans Power Electron* 1995;**10**(6):659–65.
8. Balestrino A, Corsanini D, Landi A, Sani L. Circle-based criteria for performance evaluation of controlled DC–DC switching converters. *IEEE Trans Ind Electron* 2006;**53**(6):767–70.
9. Veerachary M. Analysis of fourth-order DC–DC converters: a flow graph approach. *IEEE Trans Ind Electron* 2008;**55**(1):133–41.
10. Tymerski R, Li DW. Extended ripple analysis of PWM DC–DC converters. *IEEE Trans Power Electron* 1993;**8**(4):588–95.
11. Tymerski RP, Vorperian V, Lee FCY, Baumann WT. Nonlinear modeling of the PWM switch. *IEEE Trans Power Electron* 1989;**4**(2):225–33.
12. Krein PT, Bentsman J, Bass RM, Lesieutre BC. On the use of averaging for the analysis of power electronic systems. *IEEE Trans Power Electron* 1990;**5**(2):621–6.
13. Tymerski R. Volterra series modeling of power conversion systems. *IEEE Trans Power Electron* 1991;**6**(4):712–8.
14. Chung HSH, Ionovici A, Zhang J. Describing functions of power electronics circuits using progressive analysis of circuit waveforms. *IEEE Trans Circuits Syst Fundam Theory Appl* 2000;**47**(7):1026–37.
15. Tse CKM, Adams KM. Quasi-linear modeling and control of DC–DC converters. *IEEE Trans Power Electron* 1992;**7**(2):315–23.
16. Hsieh FH, Yen NZ, Juang YT. Optimal controller of a buck DC–DC converter using the uncertain load as stochastic noise. *IEEE Trans Circuits Syst Express Briefs* 2005;**52**(2):77–81.
17. Jeltsema D, Scherpen JMA. Tuning of passivity-preserving controllers for switched-mode power converters. *IEEE Trans Autom Control* 2004;**49**(8):1333–44.

18. Gensior A, Woywode O, Rudolph J, Güldner H. On differential flatness, trajectory planning, observers, and stabilization for DC–DC converters. *IEEE Trans Circuits Syst Regul Pap* 2006;**53**(9):2000–10.
19. Naim R, Weiss G, Ben-Yaakov S. H^{∞} control applied to boost power converters. *IEEE Trans Power Electron* 1997;**12**(4): 677–83.
20. Kugi A, Schlacher K. Nonlinear H_{∞}-controller design for a DC-to-DC power converter. *IEEE Trans Control Syst Technol* 1999;**7**(2):230–7.
21. Cervantes I, Garcia D, Noriega D. Linear multiloop control of quasi-resonant converters. *IEEE Trans Power Electron* 2004;**18**(5):205–22.
22. Frank HFL, Peter KST, Li CK. An improved LQR-based controller for switching DC–DC converters. *IEEE Trans Ind Electron* 1993;**40**(5):521–8.
23. Hsieh CY, Chen KH. Adaptive pole-zero position (APZP) technique of regulated power supply for improving SNR. *IEEE Trans Power Electron* 2008;**23**(6):2949–63.
24. Lam HK, Tan SC. Stability analysis of fuzzy-model-based control systems: application on regulation of switching DC–DC converter. *IET Control Theory Appl* 2009;**3**(8):1093–106.
25. Perry AG, Feng G, Liu YF, Sen PC. A design method for PI-like fuzzy logic controllers for DC–DC converter. *IEEE Trans Ind Electron* 2007;**54**(5):2688–96.
26. Sira-Ramirez H, Garcia-Esteban M, Zinober ASI. Dynamical adaptive pulse-width modulation control of DC–DC power converters: a backstepping approach. *Int J Control* 1996;**65**(2):205–22.
27. Sira-Ramirez H. Differential geometric methods in variable-structure control. *Int J Control* 1988;**48**(4):1359–90.
28. Lin DX, Zheng YL. VSC buck converter for DC motor speed regulation. *J Fujian Univ Technol* 2006;**4**(3):338–42 [Chinese].
29. Zhou XX, Fang JC, Liu G. Variable structure control strategy research on the magnetically suspended reaction flywheel. *Electr Mach Control* 2008;**12**(5):487–92 [Chinese].
30. Wang YN, Zhang XZ, Yuan XF, Liu GR. Position-sensorless hybrid sliding-mode control of electric vehicles with brushless DC motor. *IEEE Trans Veh Technol* 2011;**60**(2):421–32.
31. Hu QL, Zhang YM, Huo X, Xiao B. Adaptive integral-type sliding mode control for spacecraft attitude maneuvering under actuator stuck failures. *Chin J Aeronaut* 2011;**24**(1):32–45.
32. Jin YQ, Liu XD, Qiu W, Hou CZ. Time-varying sliding mode controls in rigid spacecraft attitude tracking. *Chin J Aeronaut* 2008;**21**(4):352–60.
33. Sira-Ramirez H. A geometric approach to pulse-width modulated control in nonlinear dynamical systems. *IEEE Trans Autom Control* 1989;**34**(2):184–7.
34. Sira-Ramirez H. Sliding motions in bilinear switched networks. *IEEE Trans Circuits Syst* 1987;**34**(8):919–33.

Liu Gang received his B.E. and M.E. degrees from Shandong University in 1992 and 1998 respectively, and Ph.D. degree from Dalian University of Technology in 2001. He is currently a professor and Ph.D. advisor in the School of Instrumentation Science and Opto-electronics Engineering at Beihang University. His main research interests are spacecraft attitude control, precision mechanical and electrical control systems.

Zhang Cong received his B.E. degree from University of Electronics Science and Technology of China in 2005 and M.E. degree from China Precision Engineering Institute for Aircraft Industry in 2008. He is currently a Ph.D. student in the School of Instrumentation Science and Opto-electronics Engineering at Beihang University. His main research interests are motor drive and control technologies for spacecraft actuators.